Floquet Modulation for Measuring Probe-Induced Shifts in Optical Lattice Clocks*

Ruo-Shui Han(韩弱水)[1] and Yan-Hua Zhou(周彦桦)[2†]

[1]Department of Physics and Chongqing Key Laboratory for Strongly Coupled Physics, Chongqing University, Chongqing, 401331, China

[2]National Time Service Center, Chinese Academy of Sciences, Xi'an, Shaanxi, 710600, China

October 13, 2026

Abstract

We investigate Floquet modulation for measuring the probe-induced AC Stark shift coefficient in optical lattice clocks. Periodic frequency modulation allows a high probe intensity to enlarge the measured frequency difference between the settings at low and high probe power while Bessel function dressing maintains a narrow excitation spectrum. This combination improves sensitivity to the coefficient without sacrificing frequency discrimination. We identify modulation conditions that suppress additional frequency shifts while avoiding strong motional resonances. At the same probe intensities and total measurement time, numerical simulations including preparation time show a lower coefficient uncertainty than conventional Rabi interrogation with a single π pulse. At high probe intensities, the Floquet coefficient uncertainty approaches a plateau dominated by Rabi frequency calibration.

Keywords: Optical lattice clocks; Floquet modulation; probe-induced AC Stark shift

PACS: 06.30.Ft; 32.60.+i; 37.10.Jk; 42.50.Nn;

1. Introduction

Optical lattice clocks (OLCs) based on ultracold neutral atoms and ultranarrow transitions have reached systematic fractional frequency uncertainties at the 10^{-18} to 10^{-19} levels [1–10]. Beyond timekeeping, optical clocks have enabled applications in relativistic geodesy [4,9], searches for variations of fundamental constants [11,12], and precision tests of fundamental physics [12–14]. Probe-induced AC Stark shifts are already precisely evaluated and strongly suppressed in OLCs. Further progress toward the 10^{-20} regime motivates more precise characterization of residual probe-induced frequency shifts.

Rabi excitation with larger pulse areas changes the fringe structure, and Ramsey sequences permit narrow fringes with short, intense pulses. Hyper-Ramsey and autobalanced Ramsey spectroscopy suppress probe-

*Project supported by the National Natural Science Foundation of China (Grant No. 12274045).

†Corresponding author. E-mail: 850802208@qq.com

induced AC Stark shifts in the clock output [15–20]. Calibrated auxiliary observables or compensation signals can also provide probe shift information.

Power extrapolation uses clock measurements at multiple probe intensities to evaluate these shifts [21]. Increasing the difference between the low and high probe intensities enlarges the measured frequency difference because the shift scales with intensity. For a given uncertainty in this frequency difference, the larger measurement lever reduces the statistical uncertainty of the extracted shift coefficient. For conventional Rabi interrogation, however, higher probe power requires a shorter π pulse. The resulting broader spectrum reduces frequency discrimination and offsets part of the gain from the larger measurement lever.

Floquet engineering provides an additional degree of control over coherent dynamics through effective Hamiltonians [22–27]. Periodic frequency modulation controls the effective Rabi frequency through Bessel function dressing [22,28]. A small effective Rabi frequency then permits a long interrogation pulse and a narrow spectrum at high probe power. Related interrogation techniques using Floquet engineering, frequency modulation, and strong driving have also been investigated in OLCs and precision spectroscopy [28–33]. Xu *et al.* [28] experimentally used this frequency modulation principle to measure the probe Stark shift in a ^{87}Sr optical lattice clock with an enlarged measurement lever.

Applying this principle to precise coefficient measurements requires control of finite-frequency shifts and motional excitation. Finite-frequency corrections to the zeroth-order Hamiltonian can distort the spectrum and shift the measured line center. We define the Floquet-engineered (FE) frequency shift as the measured line center minus the transition frequency including the probe-induced AC Stark shift. This shift depends on the modulation frequency, depth, and initial phase. Micromotion-induced shifts in periodically driven OLCs have recently been investigated theoretically and experimentally, and a dual-modulation scheme has been developed to suppress them [34]. Floquet-assisted transitions between external motional states can also distort the spectrum when the modulation satisfies motional resonance conditions.

We evaluate the uncertainty of the probe shift coefficient obtained from measurements at two probe powers, accounting for modulation-induced shifts and control errors. We examine finite-frequency shifts and motional resonances to select the modulation phase and frequency. The uncertainty budget combines statistical frequency noise with fluctuations in pulse parameters and uncertainty in the Rabi frequency calibration. Our numerical comparison shows that Floquet modulation yields a lower coefficient uncertainty than conventional Rabi interrogation with a single π pulse at the same probe intensities and total measurement time, including the time required to prepare the atoms for each probe pulse.

Section 2 presents the measurement principle. Section 3 examines finite-frequency shifts and motional excitation to guide the choice of modulation phase and frequency. Section 4 compares the coefficient uncertainties of the two interrogation schemes, and Section 5 concludes the paper.

2. Principle of Floquet-Enhanced Measurement of Probe-Induced AC Stark Shifts

Measurements of the probe shift coefficient benefit from a large measurable frequency difference and a narrow excitation spectrum. The probe-induced shift is proportional to the probe intensity, or equivalently to

the squared bare Rabi frequency. We write

$$\delta\nu_{\mathrm{probe}} = C_{\mathrm{probe}}\Omega_0^2, \tag{1}$$

where C_{probe} is the probe shift coefficient and Ω_0 is the angular bare Rabi frequency, which quantifies the atom–light coupling strength at the given probe intensity. We define $\delta\nu_{\mathrm{probe}}$ as the perturbed transition frequency minus the unperturbed transition frequency, expressed in hertz. With Ω_0 in radians per second, C_{probe} has units of $\mathrm{Hz\,s^2/rad^2}$.

In practice, the coefficient is determined by interrogating the atoms at low and high probe powers. We denote the corresponding nominal bare Rabi frequencies by Ω_{low} and Ω_{high}, and the value at the clock's normal operating intensity by Ω_{op}. Here, a nominal value is the set value relative to which fluctuations and calibration errors are defined. We define the difference between the squared Rabi frequencies as $\Delta\Omega^2 = \Omega_{\mathrm{high}}^2 - \Omega_{\mathrm{low}}^2$. For a frequency difference arising from the probe-induced AC Stark shift alone, the shift at the normal operating intensity is

$$\delta\nu_{\mathrm{probe,op}} = C_{\mathrm{probe}}\Omega_{\mathrm{op}}^2 = \frac{\langle\delta\nu_{\mathrm{lock-in}}\rangle\Omega_{\mathrm{op}}^2}{\Delta\Omega^2} = \frac{\langle\delta\nu_{\mathrm{lock-in}}\rangle}{\mathcal{L}}, \tag{2}$$

where $\langle\delta\nu_{\mathrm{lock-in}}\rangle = \langle\nu_{\mathrm{high}}\rangle - \langle\nu_{\mathrm{low}}\rangle$ is the mean measured frequency difference between the two probe powers. The quantity $\mathcal{L} = \Delta\Omega^2/\Omega_{\mathrm{op}}^2$ is the dimensionless measurement lever for this operating point. Section 4 includes additional spectral offsets and mean shifts caused by parameter fluctuations.

At fixed Ω_{op}, increasing $\Delta\Omega^2$ enlarges the measurement lever $\mathcal{L}$, as illustrated in Fig. 1(a). Because Ω_{low}^2 is bounded below by zero, the gain from reducing Ω_{low} is limited. We therefore enlarge the difference mainly by increasing Ω_{high}. For a given measurement uncertainty in $\langle\delta\nu_{\mathrm{lock-in}}\rangle$, Eq. (2) then gives a smaller statistical uncertainty in the inferred probe shift at the normal operating point.

For conventional Rabi interrogation with a single π pulse, increasing Ω_{high} shortens the pulse at high probe power to $t = \pi/\Omega_{\mathrm{high}}$ and broadens the Fourier-limited Rabi spectrum. This broadening reduces frequency discrimination and offsets part of the gain from the larger measurement lever. To retain a narrow excitation spectrum at high probe intensity, we modulate the probe laser frequency as

$$\omega_p(t) = \omega_c - A\omega_s\cos(\omega_s t + \phi), \tag{3}$$

where $\omega_p(t)$ is the probe angular frequency and ω_c is its carrier angular frequency. The modulation parameters are the dimensionless depth A, angular frequency ω_s (with $\nu_s = \omega_s/(2\pi)$ in hertz), and initial phase ϕ.

In the ideal high-frequency limit, the two-level dynamics in a periodic rotating frame are described by the zeroth-order Floquet Hamiltonian [23,28,34]

$$H_F^{(0)} = -\frac{\hbar\tilde{\delta}}{2}\sigma_z + \frac{\hbar\Omega_{\mathrm{eff}}}{2}\sigma_x, \tag{4}$$

where $\hbar = h/(2\pi)$ is the reduced Planck constant, and σ_x, σ_y, and σ_z are the Pauli matrices. We define $\delta = \omega_c - \omega_0$ as the angular detuning from the unperturbed clock transition, whose angular frequency is ω_0. Including the probe-induced AC Stark shift gives $\tilde{\delta} = \delta - 2\pi\delta\nu_{\mathrm{probe}}$. The effective Rabi frequency is given by $\Omega_{\mathrm{eff}} = \Omega_0 J_0(A)$, where J_l denotes the Bessel function of the first kind of order l. Increasing Ω_{high} enlarges the measurement lever, while adjusting A keeps the effective Rabi frequency small at high probe power. This permits a long interrogation time and a narrow spectrum, as illustrated by the comparison at high probe power

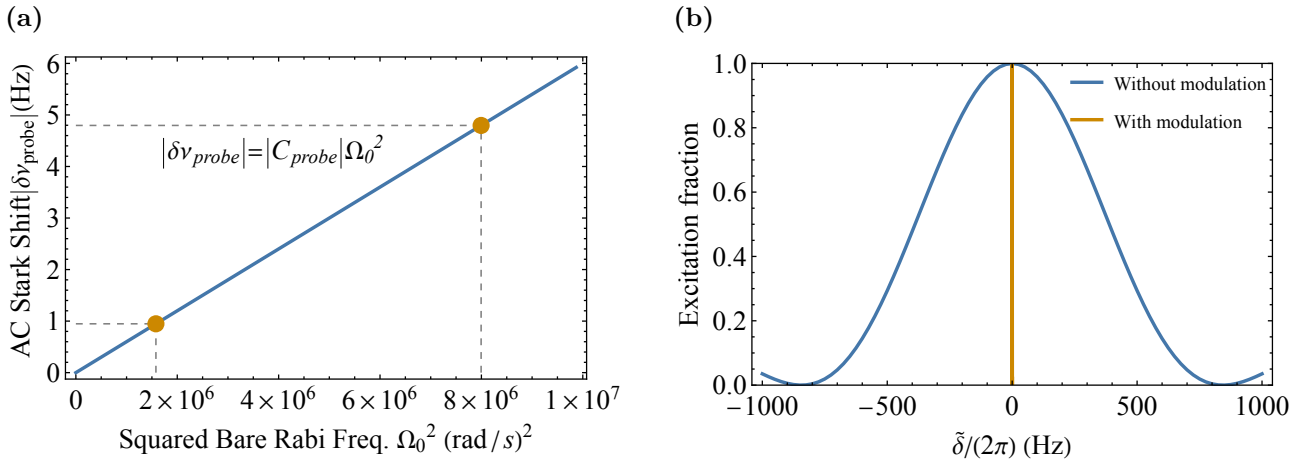


Figure 1: Principle of Floquet-enhanced measurement of probe-induced AC Stark shifts. (a) The magnitude of the probe-induced AC Stark shift is proportional to the squared bare Rabi frequency, $|\delta\nu_{\mathrm{probe}}| = |C_{\mathrm{probe}}|\Omega_0^2$. The orange circles mark the measurement points at low and high probe power, and the gray dashed lines indicate their coordinates. A larger separation between these points along the Ω_0^2 axis increases the magnitude of the difference in clock frequency. (b) At the same high probe power, Floquet modulation reduces the effective coupling and allows a longer interrogation pulse and a narrower excitation spectrum than conventional Rabi interrogation with a single π pulse.

in Fig. 1b. Therefore, Floquet modulation provides a route to enhance the probe shift measurement without sacrificing spectroscopic resolution. The derivation of Eq. (4) is given in Appendix A.

Pure frequency modulation redistributes probe power among sidebands while preserving the total intensity. The frequency dependence of the differential polarizability across these sidebands can change the probe shift coefficient. The scalar background polarizability model in Appendix B gives a negligible relative correction over the modulation range considered here, so we use the unmodulated C_{probe}.

Although the zeroth-order Floquet picture explains the narrow excitation spectrum at high probe intensity, the periodic drive introduces additional effects that must be assessed when choosing the modulation parameters. The first is micromotion, which has been shown to distort the excitation spectrum and produce frequency shifts in periodically driven OLCs [34].

The second is Floquet-assisted motional excitation, which can modify the spectrum through transitions between motional states. Its contribution depends on the trapping conditions and the motional state distribution.

In the following section, we first study the dependence of the micromotion-induced FE shift on the initial modulation phase. We then examine Floquet-assisted motional excitation and evaluate how thermal averaging affects the resulting frequency shift. These analyses guide the choice of operating parameters for measuring probe-induced AC Stark shifts.

3. Micromotion Shifts and Motional Excitation

We consider an ensemble of clock atoms trapped in a one-dimensional optical lattice operated at the magic wavelength [35]. The lattice is sufficiently deep to suppress intersite tunneling. For these ultracold atoms, we

describe motion within each lattice site in a three-dimensional harmonic oscillator basis. The radial trapping frequencies are on the order of hundreds of hertz, whereas the axial frequency is on the order of tens of kilohertz. The clock laser couples the two clock states with the same nuclear spin projection. We retain the dependence of the coupling matrix elements on the probe direction and use perfect alignment with the lattice axis for the numerical results below. With the probe frequency modulation in Eq. (3), the system Hamiltonian is

$$\begin{aligned}\hat{H}(t)/\hbar = &\sum_{\mathbf{n}} \frac{E_{\mathbf{n}}}{\hbar} \left(|e,\mathbf{n}\rangle\langle e,\mathbf{n}| + |g,\mathbf{n}\rangle\langle g,\mathbf{n}|\right) \\ &- \frac{\tilde{\delta} - A\omega_s \cos(\omega_s t + \phi)}{2} \sum_{\mathbf{n}} \left(|e,\mathbf{n}\rangle\langle e,\mathbf{n}| - |g,\mathbf{n}\rangle\langle g,\mathbf{n}|\right) \\ &+ \sum_{\mathbf{n},\mathbf{m}} \left[\frac{\Omega_{\mathbf{nm}}}{2}|e,\mathbf{n}\rangle\langle g,\mathbf{m}| + \frac{\Omega^*_{\mathbf{nm}}}{2}|g,\mathbf{m}\rangle\langle e,\mathbf{n}|\right]. \end{aligned} \tag{5}$$

Here, $\mathbf{n} = (n_x, n_y, n_z)$ and $\mathbf{m} = (m_x, m_y, m_z)$ label motional harmonic oscillator states. The z direction is defined along the optical lattice axis, whereas the x direction is transverse to the lattice axis and lies in the plane formed by the lattice and probe beams. The probe wave vector has no component along y, so n_y is conserved during interrogation. The contribution of n_y to the motional energies and thermal weights is retained. The states $|g\rangle$ and $|e\rangle$ denote the $^1S_0$ and $^3P_0$ clock states, respectively. The motional energy $E_{\mathbf{n}}$ includes the anharmonic and axial–radial corrections given in Appendix C. The quantity $\Omega_{\mathbf{nm}}$ is the clock laser coupling matrix element between motional states $\mathbf{m}$ and $\mathbf{n}$. Its explicit form is given in Appendix D. For long interrogation times, we choose A close to 2.4, near the first zero of $J_0(A)$, to reduce the effective carrier Rabi frequency and narrow the spectrum.

In the periodic rotating frame defined in Appendix A, we apply the high-frequency Floquet–Magnus expansion with the modulation phase defined at $t = 0$. The resulting Floquet Hamiltonian describes the stroboscopic dynamics at integer multiples of the modulation period:

$$\hat{H}_F = \hat{H}_F^{(0)} + \hat{H}_F^{(1)} + \mathrm{O}\left(\omega_s^{-2}\right). \tag{6}$$

Here, $\hat{H}_F^{(0)}$ is the zeroth-order effective Hamiltonian, and $\hat{H}_F^{(1)}$ is the leading finite-frequency correction proportional to ω_s^{-1}. The zeroth-order Hamiltonian $\hat{H}_F^{(0)}$ is

$$\begin{aligned}\hat{H}_F^{(0)}/\hbar = &\sum_{\mathbf{n}} \frac{\Delta E_{\mathbf{n}}}{\hbar} \left(|e,\mathbf{n}\rangle\langle e,\mathbf{n}| + |g,\mathbf{n}\rangle\langle g,\mathbf{n}|\right) \\ &- \sum_{\mathbf{n}} \frac{\tilde{\delta}}{2} \left(|e,\mathbf{n}\rangle\langle e,\mathbf{n}| - |g,\mathbf{n}\rangle\langle g,\mathbf{n}|\right) \\ &+ \sum_{\mathbf{n},\mathbf{m}} \frac{\Omega_{\mathbf{nm}}}{2} J_{-q_{\mathbf{nm}}} e^{-iq_{\mathbf{nm}}\phi} |e,\mathbf{n}\rangle\langle g,\mathbf{m}| + H.C. \end{aligned} \tag{7}$$

Here and below, we use the shorthand notation $J_l \equiv J_l(A)$, where l labels the Fourier component generated by the periodic modulation. For each motional state $\mathbf{n}$, the residual quasienergy is defined as $\Delta E_{\mathbf{n}} = E_{\mathbf{n}} - q_{\mathbf{n}}\hbar\omega_s$, where the integer $q_{\mathbf{n}}$ is chosen to minimize $|\Delta E_{\mathbf{n}}|$ and $q_{\mathbf{nm}} = q_{\mathbf{n}} - q_{\mathbf{m}}$. The first-order Floquet Hamiltonian contains terms within each clock state manifold and terms that modify the coupling between the clock states:

$$\begin{aligned}\hat{H}_F^{(1)}/\hbar = &\sum_{\mathbf{n},\mathbf{m}} \left[\alpha^{(e)}_{\mathbf{nm}}|e,\mathbf{n}\rangle\langle e,\mathbf{m}| + \alpha^{(g)}_{\mathbf{nm}}|g,\mathbf{n}\rangle\langle g,\mathbf{m}|\right] \\ &+ \sum_{\mathbf{n},\mathbf{m}} \left[\left(\frac{\Delta E_{\mathbf{m}} - \Delta E_{\mathbf{n}}}{\hbar} + \tilde{\delta}\right)\beta_{\mathbf{nm}}|e,\mathbf{n}\rangle\langle g,\mathbf{m}| + \mathrm{H.c.}\right]. \end{aligned} \tag{8}$$

The full expressions for $\alpha_{\mathbf{nm}}^{(e,g)}$ and $\beta_{\mathbf{nm}}$ are given in Appendix A.

The coefficients $\alpha_{\mathbf{nm}}^{(e,g)}$ are quadratic in the probe coupling and describe processes through intermediate motional states $\mathbf{p}$. To identify the phase dependence of the carrier response, we first adopt the carrier approximation, retaining $\mathbf{n} = \mathbf{m}$ and $\mathbf{p} = \mathbf{n}$. Using $J_{-l} = (-1)^l J_l$, we find that the carrier contributions at $\phi = \pi/2$ satisfy $\alpha_{\mathbf{nn}}^{(e)} = \alpha_{\mathbf{nn}}^{(g)} = 0$.

The coefficient $\beta_{\mathbf{nm}}$ corrects the coupling between the clock states and introduces a detuning-dependent modification of the Rabi frequency. For the carrier transition with $\boldsymbol{n} = \boldsymbol{m}$, one has $q_{\mathbf{nn}} = 0$, and Eq. (30) becomes

$$\beta_{\mathbf{nn}} = \sum_{l=1}^{\infty} \frac{\Omega_{\mathbf{nn}} J_l}{2\omega_s l} \left[(-1)^l e^{-il\phi} - e^{il\phi}\right]. \tag{9}$$

At $\phi = \pi/2$, the two phase-dependent terms cancel exactly, giving $\beta_{\mathbf{nn}} = 0$. Since both the diagonal and coupling corrections vanish in the carrier approximation at $\phi = \pi/2$, this phase suppresses the leading micromotion-induced FE shift.

To model the experimental measurement, we determine the FE shift from two sampling points on opposite flanks of the selected central resonance. The points have a fixed frequency separation and equal excitation probabilities, and their midpoint gives the shift:

$$P(\nu_L) = P(\nu_R), \qquad \nu_R - \nu_L = 2\nu_{\text{off}}, \qquad \delta\nu_{\text{FE}} = \frac{\nu_L + \nu_R}{2}. \tag{10}$$

Here, $P(\nu)$ is the excitation probability for the clock transition at the end of the pulse. The sampling frequencies ν_L and ν_R are values of the detuning $\nu = \tilde{\delta}/(2\pi)$, measured relative to the probe-shifted transition. The sampling offset is fixed at the half-width at half maximum of an ideal Rabi π-pulse with the chosen interrogation time: $\nu_{\text{off}} = \kappa/t$, with $\kappa \simeq 0.39934$. Thus, $\nu_{\text{off}} \simeq 0.39934$ Hz for $t = 1$ s. We keep this offset unchanged across scans at the same interrogation time and during noise propagation.

We test the predicted phase dependence by numerically calculating the spectra from Eq. (5) for different initial modulation phases, as shown in Fig. 2a. The atoms are initially prepared in $|g, n_z = 0, n_r = 0\rangle$, where $n_r = n_x + n_y$ labels the radial shell. The detuning is scanned across the central Rabi resonance without thermal averaging. For Fig. 2a, we fix the bare Rabi and modulation frequencies at $\Omega_0 = 1500 \times 2\pi$ rad/s and $\omega_s = 10000 \times 2\pi$ rad/s, respectively. For a π-pulse duration $t_\pi = 1$ s, we select $A = 2.39954$ numerically from the full time-dependent Hamiltonian and use these parameters for all phases. With the chosen interrogation time and modulation frequency, the pulse contains an integer number of modulation periods, so the system is observed stroboscopically.

Away from $\phi = \pi/2$, finite-frequency corrections distort the Rabi spectrum and produce a micromotion-induced frequency shift. At $\phi = \pi/2$, the spectrum remains nearly symmetric around zero detuning, consistent with the carrier cancellation.

We then examine the phase dependence across probe powers in a separate scan at fixed $A = 2.2$, as shown in Fig. 2b. The pulse duration is adjusted with probe power and restricted to an integer number of modulation periods. At each power, the same duration is used for all phases. The FE shift varies approximately linearly with Ω_0^2/ω_s, with the fitted slope strongly suppressed at $\phi = \pi/2$. At fixed modulation frequency, this power-dependent shift contributes, along with the probe Stark shift, to the measured frequency difference between the two probe powers. Its suppression, consistent with the first-order carrier cancellation, supports the choice $\phi = \pi/2$. Appendix C gives the sampling, fitting, and numerical verification details.

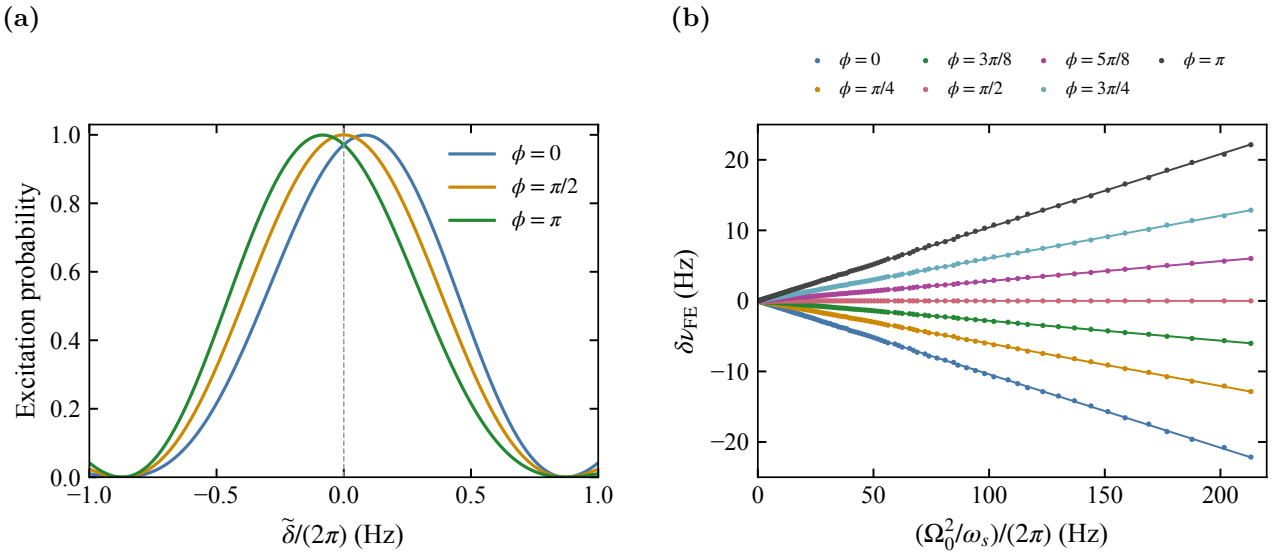


Figure 2: Micromotion-induced spectral distortion and frequency shift under Floquet modulation. (a) Rabi excitation spectra for different initial modulation phases ϕ, calculated with the bare Rabi frequency $\Omega_0 = 1500 \times 2\pi$ rad/s, modulation frequency $\omega_s = 10000 \times 2\pi$ rad/s, modulation depth $A = 2.39954$, and a π-pulse duration $t_\pi = 1$ s determined numerically from the full time-dependent Hamiltonian. The spectra for $\phi = 0$ and $\phi = \pi$ are shifted in opposite directions, whereas the spectrum for $\phi = \pi/2$ remains nearly centered at zero detuning. (b) FE shift as a function of $(\Omega_0^2/\omega_s)/(2\pi)$ for different initial modulation phases. The modulation frequency is fixed at $\omega_s = 10000 \times 2\pi$ rad/s, while the bare Rabi frequency settings are selected from a scan spanning $\Omega_0 = 100 \times 2\pi$ rad/s to $1500 \times 2\pi$ rad/s. The modulation depth is fixed at $A = 2.2$, and the pulse contains an integer number of modulation periods, with the same duration for every phase at a given Ω_0. The markers represent the numerical results, and the solid lines are linear fits. The dimensionless fitted slope $k_{\pi/2}$ at $\phi = \pi/2$ obeys $|k_{\pi/2}| < 10^{-6}$ for this scan. Phases symmetrically located about $\phi = \pi/2$ exhibit slopes of approximately equal magnitude and opposite sign.

Choosing $\phi = \pi/2$ suppresses the leading carrier correction, while the zeroth-order Hamiltonian in Eq. (7) retains couplings between different motional states. We now examine how these couplings constrain the modulation frequency. The coupling between $|g, \mathbf{m}\rangle$ and $|e, \mathbf{n}\rangle$ is given by $\Omega_{\mathbf{nm}} J_{-q_{\mathbf{nm}}} e^{-iq_{\mathbf{nm}}\phi}/2$, while their quasienergy separation near zero detuning is determined by $(\Delta E_{\mathbf{n}} - \Delta E_{\mathbf{m}})/\hbar$. Away from motional resonances, these transitions are suppressed when their coupling is weak compared with the residual quasienergy mismatch. However, when the modulation frequency satisfies the resonance condition

$$q_{\mathbf{nm}}\omega_s \simeq \frac{E_{\mathbf{n}} - E_{\mathbf{m}}}{\hbar}, \tag{11}$$

the residual quasienergies of the two motional states become nearly degenerate, i.e., $\Delta E_{\mathbf{n}} \simeq \Delta E_{\mathbf{m}}$, and Floquet photons can bridge the motional energy difference. Consequently, the transition between motional states becomes resonantly enhanced and can strongly distort the clock Rabi spectrum.

The spectra near four-, three- and two-photon motional resonances are shown in Fig. 3a. For each case, we choose A to obtain a π-pulse duration of $t_\pi = 1$ s. The three frequencies have the same small positive residual detuning from their corresponding motional resonances. The four-photon spectrum retains a distinct central peak with side lobes, whereas the three-photon spectrum is substantially broadened and the two-photon

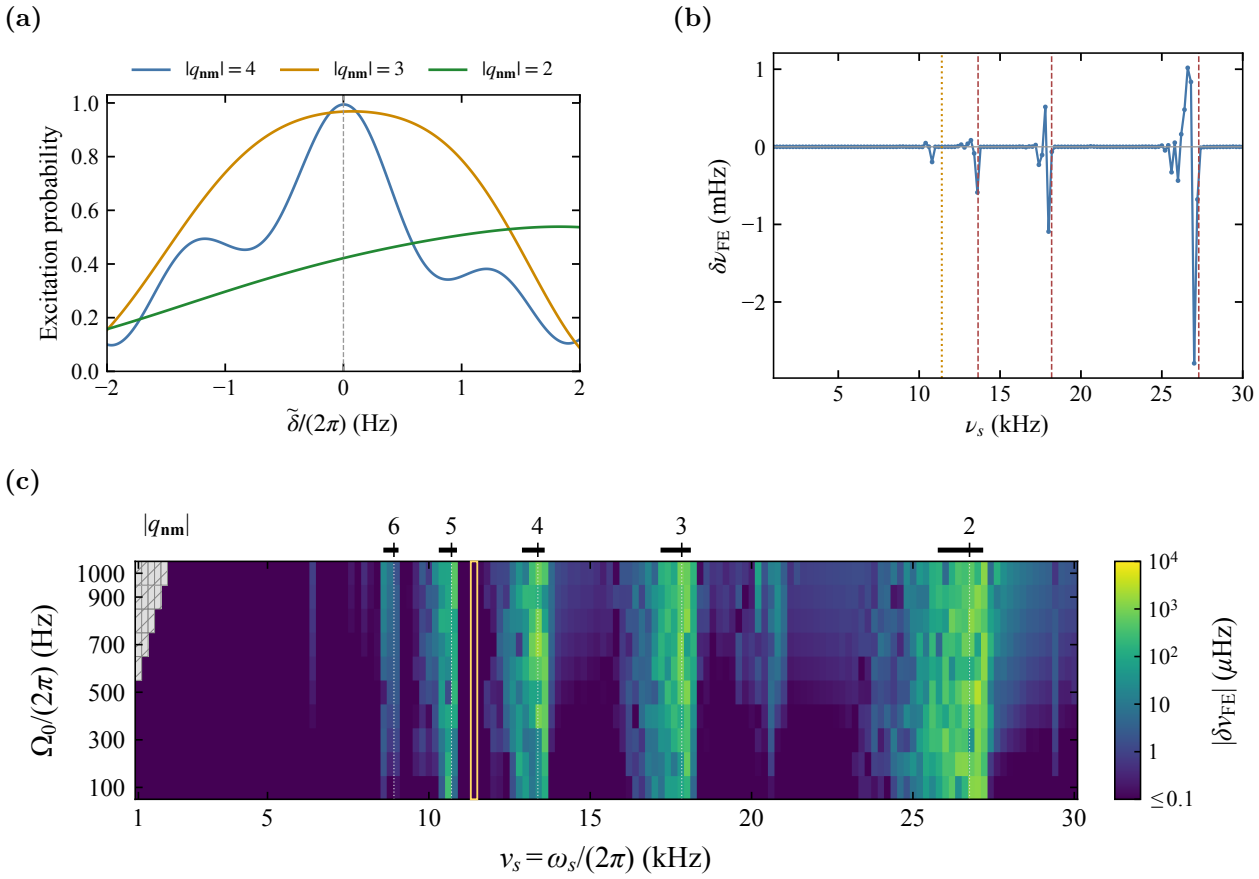


Figure 3: Floquet-assisted motional excitation and FE frequency shifts. (a) Rabi spectra near three representative resonances between motional states, corresponding to $|q_{\mathbf{nm}}| = 4$, $|q_{\mathbf{nm}}| = 3$, and $|q_{\mathbf{nm}}| = 2$. The calculations are performed with $\phi = \pi/2$ and $\Omega_0 = 500 \times 2\pi$ rad/s. The atoms are initially prepared in $|g, n_z = 0, n_r = 0\rangle$, and the motional resonance couples this state to $|e, n_z = 1, n_r = 0\rangle$. For $|q_{\mathbf{nm}}| = 4, 3, 2$, respectively, the modulation frequencies are $\nu_s = 13644, 18192, 27288$ Hz and the modulation depths are $A = 2.40106, 2.40236, 2.40173$, with a π-pulse duration of $t_\pi = 1$ s. The spectra illustrate how Floquet-assisted motional excitation reshapes the clock response near these resonances. (b) FE shift extracted from the thermally averaged excitation spectrum as a function of the modulation frequency. The initial modulation phase and bare Rabi frequency are fixed at $\phi = \pi/2$ and $\Omega_0 = 500 \times 2\pi$ rad/s, respectively, while the modulation frequency is scanned from $\omega_s = 1000 \times 2\pi$ rad/s to $30000 \times 2\pi$ rad/s. At each scan point, we locally optimize A to maximize the thermally averaged central peak at fixed $t = 1$ s. The initial axial state is $n_z = 0$, and radial shells n_r are averaged at radial temperature $T_r = 0.5$ μK using the weights in Appendix C. The red dashed lines indicate representative resonance conditions with $|q_{\mathbf{nm}}| = 4$, 3, and 2. The orange dotted line marks the selected modulation frequency $\nu_s = 11.4$ kHz. Outside the regions affected by motional resonances, the FE shift remains close to zero. (c) Two-dimensional map of $|\delta\nu_{\mathrm{FE}}|$ under ideal probe–lattice alignment, $\Delta\theta = 0$, with the FE shift extracted from the thermally averaged excitation spectrum at $\phi = \pi/2$, $T_r = 0.5$ μK, and $t = 1$ s. The modulation depth is locally optimized at each point. The yellow outline marks the working points at $\nu_s = 11.4$ kHz. The logarithmic color scale has a 0.1 μHz display floor; cells show the sampled values without interpolation. Hatching excludes $\Omega_0/\omega_s > 1/2$. Dotted lines provide guides to energy matching for $n_z = 0 \to 1$ at the indicated $|q_{\mathbf{nm}}|$. The upper bars show the 5th–95th percentile range of these matching frequencies across the radial thermal distribution.

spectrum no longer has a distinct central peak.

For a fixed motional energy spacing, lowering the modulation frequency accesses higher-order resonances, whose couplings are weaker because the corresponding Bessel coefficients $J_{q_{\mathbf{nm}}}(A)$ are smaller for the values of A considered here. However, lowering the modulation frequency also increases finite-frequency corrections, which scale as ω_s^{-r} at order r. We therefore choose a modulation frequency high enough to suppress these corrections while avoiding strong motional resonances.

For the Floquet sidebands and motional couplings discussed above, the following conditions provide qualitative guidance for choosing the modulation frequency:

$$\max_{l\neq 0} \frac{\Omega_0 |J_l(A)|}{\omega_s} \ll 1, \qquad \left| q_{\mathbf{nm}}\omega_s - \frac{E_{\mathbf{n}} - E_{\mathbf{m}}}{\hbar} \right| \gg |\Omega_{\mathbf{nm}} J_{q_{\mathbf{nm}}}(A)| \,. \tag{12}$$

The first condition requires the nonzero sideband couplings to be weak relative to the modulation frequency. For transitions from thermally populated states to other motional states ($\mathbf{n} \neq \mathbf{m}$), the second condition requires the residual detuning to be much larger than the coupling strength. We determine the residual spectral shift from the full time-dependent model.

To identify suitable operating frequencies, we scan ω_s from $1000 \times 2\pi$ rad/s to $30000 \times 2\pi$ rad/s. We fix $\phi = \pi/2$ and $\Omega_0 = 500 \times 2\pi$ rad/s; Fig. 3b shows the resulting FE shift. The axial–radial coupling makes the axial energy spacing depend on the radial shell n_r. In this model, perfect probe alignment prevents transitions between radial states but does not remove this dependence. We calculate the spectra for atoms initially in $n_z = 0$ and average over radial shells at $T_r = 0.5$ μK using the Boltzmann weights given in Appendix C. All shells share the same modulation depth. From the thermally averaged spectrum, we determine the peak height and extract the center using the two-point method with a fixed sampling offset.

At each modulation frequency, we optimize the common modulation depth A to maximize the local central peak of the thermally averaged spectrum at fixed $t = 1$ s. Although the ideal two-level relation $|\Omega_0 J_0(A)|t = \pi$ gives a modulation depth independent of ω_s, finite-frequency corrections and motional couplings make the numerical optimum depend on ω_s. Appendix C describes the optimization and convergence checks.

The red dashed lines in Fig. 3b indicate the representative resonance conditions with $|q_{\mathbf{nm}}| = 4$, 3, and 2. Different thermally populated radial shells have different axial energy spacings and resonance frequencies. Averaging their excitation spectra spreads the motional resonance response over a range of modulation frequencies. The FE shift extracted from this average still deviates from zero near the conditions marked by the red dashed lines. Outside the regions affected by these motional resonances, the FE shift remains close to zero, in agreement with the preceding Floquet analysis.

Because the probe shift measurement compares different probe powers, we extend the modulation frequency scan across powers to identify settings that maintain a small FE shift over the relevant power range. Figure 3c shows the deterministic bias $|\delta\nu_{\mathrm{FE}}|$ over $\Omega_0/(2\pi) = 100$–1000 Hz and $\nu_s = 1$–30 kHz. The modulation depth A is locally optimized at each point for fixed $t = 1$ s.

At $\nu_s = 11.4$ kHz, the absolute FE shifts across the sampled powers remain below 0.11 μHz, including the numerical uncertainty in locating the centers, and the peak excitation probabilities exceed 0.99998.

These results are obtained under ideal probe–lattice alignment, $\Delta\theta = 0$. A finite angular mismatch activates radial and mixed axial–radial transitions through the coupling matrix elements in Appendix D, potentially introducing additional Floquet-assisted resonances. For sufficiently small misalignment, these couplings are

expected to give perturbative corrections away from resonance, but they can modify the spectrum and FE shift near resonance. The suitability of the selected working point at $\nu_s = 11.4$ kHz therefore depends on the strengths and detunings of these additional couplings under the experimental alignment and motional conditions.

4. Numerical Comparison of Measurement Uncertainty in Floquet and Conventional Rabi Schemes

We compare the uncertainty of C_{probe} for Floquet-modulated interrogation and conventional Rabi interrogation with a single π pulse at the same probe intensities and total measurement time. The uncertainty budget includes measurement noise, fluctuations in the pulse parameters, and Rabi frequency calibration errors. We account for the different numbers of measurements allowed by the pulse durations and the preparation time, assuming independent noise between pulse pairs.

The probe shift coefficient is extracted from the measured frequency difference between the interrogations at low and high power. In experimental two-point interrogation, the excitation probability is measured once on each side of the central resonance. To simulate this measurement at both probe powers, we model the bare Rabi frequencies of the left and right sampling pulses as independent Gaussian variables centered on their set values. Their relative standard deviation is denoted by r_Ω. For interrogation at high power with Floquet modulation, the two sampling pulses share the same set modulation depth. The fluctuations in initial phase and modulation depth are zero-mean Gaussian variables with standard deviations σ_ϕ and σ_A, respectively. They are independent between the two sampling pulses, independent of each other, and independent of the power fluctuations.

For each pulse pair, we find the zero of the two-point error signal near the central resonance and use the corresponding frequency as the estimate. At power setting j, either high or low, we write the estimated frequency shift relative to the unperturbed clock transition as $C\Omega_j^2 + \xi_j$, with $C \equiv C_{\mathrm{probe}}$. The first term, $C\Omega_j^2 = \delta\nu_{\mathrm{probe},j}$, is the probe-induced AC Stark shift at the set power, where Ω_j is the set Rabi frequency. For Floquet interrogation, ξ_j includes the FE shift at the set parameter values and the additional shifts caused by parameter fluctuations. At each power, we average the frequency estimate over the pulse parameter fluctuations. Subtracting the low-power mean from the high-power mean gives

$$\langle \delta\nu_{\mathrm{lock-in}} \rangle = C\Delta\Omega^2 + \langle \xi_{\mathrm{high}} \rangle - \langle \xi_{\mathrm{low}} \rangle. \tag{13}$$

We estimate C_{probe} by solving Eq. (13) using the measured mean frequency difference.

The statistical frequency uncertainty at each power includes background clock noise and detection noise in the excitation probability [36]:

$$\sigma_{\nu,j} = \sqrt{[\nu_0 \sigma_{y,j}]^2 + \left(\frac{\gamma_{\mathrm{eff},j}}{\mathrm{SNR}_j}\right)^2}. \tag{14}$$

Here, $\nu_0 = \omega_0/(2\pi)$ is the unperturbed clock transition frequency, and $\sigma_{y,j}$ is the background fractional frequency noise after averaging. SNR_j denotes the detection signal-to-noise ratio after averaging at power j, and $\gamma_{\mathrm{eff},j}$ converts relative detection noise in the excitation probability into frequency uncertainty, as defined in Appendix E. For the same noise in the measured excitation probability, a steeper error signal reduces the resulting frequency uncertainty. We assume independent records at high and low power.

We use second-order error propagation to evaluate the mean offset $\langle \xi_j \rangle$ and the variance V_j of the estimated frequency due to noise in the parameters of one pulse pair. Averaging N_j independent pulse pairs at power j reduces this variance to V_j/N_j, while leaving the mean offset unchanged. This calculation retains the correlation between each pulse's Stark shift and excitation response, together with the mixed terms of the two-point estimator, as detailed in Appendix E.

Rabi frequency calibration errors are common to all pulse pairs at a given power and independent between power stages, so they do not decrease with averaging. We propagate these errors to first order. We denote the fractional calibration uncertainty by $r_{\mathrm{cal}} = \sigma_\Omega^{\mathrm{cal}}/\Omega$, where $\sigma_\Omega^{\mathrm{cal}}$ is the standard uncertainty of the Rabi frequency calibration. The resulting contribution V_{cal} to the variance of the frequency difference is given in Appendix E.

Differentiating Eq. (13) with respect to C gives the sensitivity of the mean frequency difference to this coefficient:

$$G_C = \Delta\Omega^2 + \frac{\partial}{\partial C}\big(\langle \xi_{\mathrm{high}} \rangle - \langle \xi_{\mathrm{low}} \rangle\big). \tag{15}$$

The corresponding coefficient uncertainty is

$$\sigma_{C_{\mathrm{probe}}} = \frac{1}{|G_C|}\sqrt{\sigma_{\nu,\mathrm{high}}^2 + \sigma_{\nu,\mathrm{low}}^2 + \frac{V_{\mathrm{high}}}{N_{\mathrm{high}}} + \frac{V_{\mathrm{low}}}{N_{\mathrm{low}}} + V_{\mathrm{cal}}}. \tag{16}$$

For the numerical evaluation, we consider a ^{87}Sr OLC with $\nu_0 \simeq 429$ THz. From the measured probe-induced AC Stark shift coefficient of the ^{87}Sr OLC in Ref. [28], we infer $C_{\mathrm{probe}} \simeq -6 \times 10^{-7}$ Hz s^2/rad^2. The negative sign indicates a decrease in the clock transition frequency with increasing probe intensity. In both schemes, the atoms start in the axial ground state, and we average the spectra over radial shells at $T_r = 0.5$ μK using Eq. (34). For interrogation at high power with Floquet modulation, we use $\nu_s = 11.4$ kHz. The initial phase is $\phi = \pi/2$, which suppresses the micromotion-induced FE shift.

For the low-power interrogation, we fix the bare Rabi frequency at $\Omega_{\mathrm{low}}/2\pi = 0.5$ Hz and use an unmodulated pulse lasting 1 s. The high-power Rabi frequency $\Omega_{\mathrm{high}}/(2\pi)$ is scanned from 20 to 1000 Hz. For Floquet interrogation at high probe power, we select the common modulation depth A at a local maximum of the thermally averaged central peak for fixed $t = 1$ s. The conventional reference uses $A = 0$ and the nominal π-pulse duration $t_j = \pi/\Omega_j$, set by the bare Rabi frequency. For each nominal duration, the sampling offset is fixed at $\nu_{\mathrm{off},j} = \kappa/t_j$; neither the duration nor the offset follows fluctuations between pulses.

For a fair comparison, we allocate the same total measurement time of 1000 s to each scheme, with 500 s at each probe power. At high probe power, the shorter pulses in conventional Rabi interrogation allow more measurements within the same total time. Averaging more independent measurements reduces the background frequency noise and increases the detection signal-to-noise ratio. We include 0.5 s for preparation, cooling and readout for each probe pulse. For each scheme, t_j denotes its pulse duration at power j. A left–right pulse pair therefore takes $2(t_j + 0.5\ \mathrm{s})$, giving $N_j = \lfloor 500\ \mathrm{s}/[2(t_j + 0.5\ \mathrm{s})] \rfloor$ complete pairs at each power.

We use $r_\Omega = 10^{-3}$, corresponding to a relative probe intensity fluctuation of approximately 2×10^{-3}, since the Rabi frequency is proportional to the square root of the probe intensity. These fluctuations in probe power cause noise in both the direct Stark shift and the FE shift. A trigger timing jitter of $\sigma_t = 1$ ns gives a phase uncertainty $\sigma_\phi = \omega_s \sigma_t = 2\pi \times 1.14 \times 10^{-5}$ rad. We assume an absolute standard deviation of $\sigma_A = 10^{-6}$ for the modulation depth as a stability target. We use a Rabi frequency calibration uncertainty of $r_{\mathrm{cal}} = 2\%$ for the baseline and also consider lower uncertainties of 1%, 0.5%, and 0.1%.

For a simplified uncertainty estimate, we set the Floquet background fractional frequency noise after averaging to $\sigma_{y,j} = 10^{-17}$ at both probe powers and the detection signal-to-noise ratio to $\mathrm{SNR}_j = 100$ at each sampling point. The two schemes have the same background fractional frequency noise per pulse pair and the same detection SNR per sampling pulse. Noise is independent between pulse pairs. At each power, we obtain the averaged Rabi background noise by dividing the averaged Floquet value by the square root of the ratio of Rabi to Floquet pulse pair counts. We multiply the averaged Floquet detection SNR by this factor to obtain the averaged Rabi SNR. Each scheme retains its own spectral conversion factor $\gamma_{\mathrm{eff},j}$. The main parameters used in the simulation are summarized in Table 1.

Table 1: Parameters used in the numerical simulation of the measurement uncertainty.

Parameter	Value	Description
ϕ	$\pi/2$	Initial modulation phase
ω_s	$11400 \times 2\pi$ rad/s	Modulation frequency
$\Omega_{\mathrm{low}}/2\pi$	0.5 Hz	Low-power bare Rabi frequency
$\Omega_{\mathrm{high}}/2\pi$	20–1000 Hz	High-power bare Rabi frequency
r_Ω	10^{-3}	Relative standard deviation of Rabi frequency fluctuations
r_{cal}	$2\%, 1\%, 0.5\%, 0.1\%$	Rabi frequency calibration uncertainty
t	1 s	Floquet interrogation time
A	Adjusted for each Ω_{high}	Modulation depth
σ_t	1 ns	Timing jitter of the modulation trigger
σ_ϕ	$2\pi \times 1.14 \times 10^{-5}$ rad	Initial phase uncertainty
C_{probe}	-6×10^{-7} Hz $\cdot$ s^2/rad^2	Probe-induced AC Stark shift coefficient
ν_0	429 THz	Clock transition frequency of strontium
$\sigma_{y,j}$	10^{-17}	Floquet background fractional frequency noise after averaging
SNR_j	100	Floquet detection signal-to-noise ratio after averaging
σ_A	10^{-6}	Assumed absolute standard deviation of the modulation depth
(n_z, n_r)	$n_z = 0;\ n_r = 0, \ldots, 400$	Initial motional ensemble
Total measurement time	1000 s	500 s at each probe power
Preparation time	0.5 s per pulse	Includes cooling and readout
m	$1.44315586525 \times 10^{-25}$ kg	^{87}Sr atomic mass
T_r	0.5 μK	Radial temperature

Figure 4(a) shows that Floquet interrogation gives a lower coefficient uncertainty throughout the scanned range at the same probe powers, total measurement time and Rabi frequency calibration uncertainty. Increasing the high probe power enlarges the measurement lever in both schemes. The shorter π pulses in conventional Rabi interrogation allow more measurements and reduce noise through averaging. However, their broader

spectra weaken frequency discrimination and offset part of this gain. Preparation time also limits the increase in the number of measurements. Floquet modulation maintains a narrow spectrum, so its coefficient uncertainty decreases more rapidly with probe power while statistical noise dominates.

Improving the Rabi frequency calibration lowers the plateau in the Floquet uncertainty. A higher probe power is then needed to reduce the statistical contribution to this lower level, extending the range over which increasing the probe power improves precision. The conventional Rabi uncertainty depends weakly on calibration precision because statistical noise dominates over this range. Once calibration errors dominate, improving the calibration reduces the total uncertainty more effectively than further increasing the probe power.

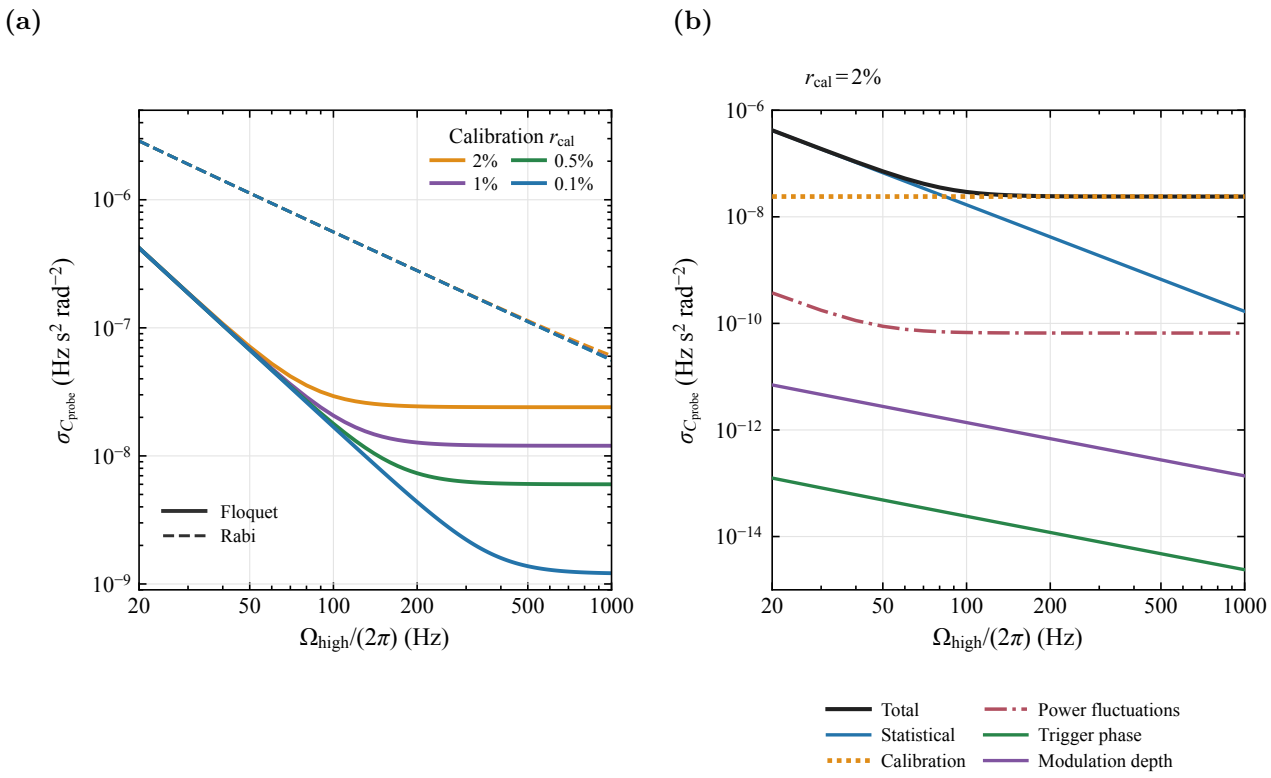


Figure 4: Uncertainty of the probe-induced AC Stark shift coefficient at the same probe intensities and total measurement time of 1000 s. (a) Floquet interrogation (solid curves) and conventional Rabi interrogation (dashed curves) at four relative Rabi frequency calibration uncertainties, indicated by color. (b) Total Floquet uncertainty and its contributions at $r_{cal} = 2\%$. Terms involving A, including mixed terms, are assigned to modulation depth; remaining phase-dependent terms are assigned to trigger phase. Both axes are logarithmic. The time is divided equally between high and low probe powers, and each probe pulse includes 0.5 s for preparation, cooling and readout. The Floquet modulation frequency is $\nu_s = 11.4$ kHz. Other parameters are given in Table 1.

Figure 4(b) shows the Floquet uncertainty contributions at $r_{cal} = 2\%$. Statistical noise dominates at low probe powers, while calibration errors dominate at high probe powers. At the assumed noise levels, modulation depth fluctuations contribute more than trigger phase fluctuations. Both contributions remain well below those from statistical noise, calibration errors and power fluctuations.

The high-power Floquet plateau is dominated by calibration uncertainty, including at $r_{\mathrm{cal}} = 0.1\%$. A useful high probe power therefore lies near the onset of the plateau and can be increased as the calibration precision improves.

5. Conclusions

In this work, we have investigated Floquet modulation as a route to improving probe-induced AC Stark shift measurements in OLCs. By using periodic frequency modulation, the bare Rabi frequency can be increased to enhance the measurement lever, while the effective Rabi frequency is reduced by Bessel function dressing to maintain a narrow spectroscopic linewidth. This avoids the spectral broadening associated with the shorter π pulse in conventional Rabi interrogation.

Choosing $\phi = \pi/2$ cancels the leading finite-frequency correction in the carrier approximation. We also showed that Floquet-assisted motional excitation can distort the excitation spectrum near motional resonances, so the modulation frequency must be selected away from strong resonances while remaining large enough to suppress finite-frequency corrections. Numerical calculations with thermal averaging identify a modulation frequency that keeps the FE shift small across the sampled probe powers.

Under these operating conditions, numerical simulations including pulse parameter fluctuations and Rabi frequency calibration uncertainty show that the Floquet scheme substantially reduces the uncertainty of the probe-induced shift coefficient C_{probe} compared with conventional Rabi interrogation with a single π pulse. Floquet modulation maintains a narrow spectrum, allowing the enlarged measurement lever to reduce the statistical contribution to the uncertainty of C_{probe}. The additional noise from trigger phase and modulation depth fluctuations does not become a dominant contribution to the coefficient uncertainty. For the equal-time comparison including preparation time, the high-power uncertainty approaches a plateau dominated by Rabi frequency calibration. The high probe power can therefore be chosen near the onset of the plateau and increased as the calibration precision improves. These results provide quantitative guidelines for choosing the modulation parameters and probe power in OLCs.

A Derivation of the Floquet Hamiltonian

In the rotating frame of the probe laser, the frequency-modulated two-level Hamiltonian is

$$\hat{H}(t) = -\frac{\hbar}{2}\left[\tilde{\delta} - A\omega_s \cos(\omega_s t + \phi)\right]\sigma_z + \frac{\hbar\Omega_0}{2}\sigma_x. \tag{17}$$

To transfer the detuning modulation to the coupling phase, we write $|\psi(t)\rangle = U(t)|\chi(t)\rangle$, with

$$U(t) = \exp\left[-i\frac{A\sin(\omega_s t + \phi)}{2}\sigma_z\right]. \tag{18}$$

The transformed Hamiltonian is

$$\hat{H}'(t) = U^\dagger(t)\hat{H}(t)U(t) - i\hbar U^\dagger(t)\frac{dU(t)}{dt}. \tag{19}$$

The second term cancels the modulation term proportional to $A\omega_s\cos(\omega_s t + \phi)$, giving

$$\hat{H}'(t) = -\frac{\hbar\tilde{\delta}}{2}\sigma_z + \frac{\hbar\Omega_0}{2}\left[\sigma_+ e^{iA\sin(\omega_s t+\phi)} + \sigma_- e^{-iA\sin(\omega_s t+\phi)}\right], \tag{20}$$

where $\sigma_\pm = (\sigma_x \pm i\sigma_y)/2$.

Using the Jacobi–Anger expansion,

$$e^{iA\sin(\omega_s t+\phi)} = \sum_{l=-\infty}^{\infty} J_l(A) e^{il(\omega_s t+\phi)}, \tag{21}$$

we separate the coupling into a time-independent carrier component and oscillating sideband components. Averaging over one modulation period retains only the $l = 0$ component and gives the zeroth-order Floquet Hamiltonian in the high-frequency approximation,

$$\hat{H}_F^{(0)} = -\frac{\hbar\tilde{\delta}}{2}\sigma_z + \frac{\hbar\Omega_0 J_0(A)}{2}(\sigma_+ + \sigma_-). \tag{22}$$

Using $\sigma_+ + \sigma_- = \sigma_x$, we recover Eq. (4).

For the motional Hamiltonian in Eq. (5), we extend this transformation to $|\psi(t)\rangle = R(t)|\chi(t)\rangle$ in the motional basis. The diagonal elements of $R(t)$ are

$$R_{s,\mathbf{n}}(t) = \exp[-iq_{\mathbf{n}}\omega_s t - isA\sin(\omega_s t+\phi)/2], \tag{23}$$

where $s = +1$ for e and $s = -1$ for g, and $q_{\mathbf{n}}$ is the integer defined in Sec. 3. The transformed Hamiltonian, expressed in angular frequency units, has Fourier components

$$\widetilde{K}(t) = R^\dagger(t)\hat{H}(t)R(t)/\hbar - iR^\dagger(t)\dot{R}(t) = \sum_l K_l e^{il\omega_s t}, \tag{24}$$

$$K_l = \begin{pmatrix} 0 & B_l \\ B_{-l}^\dagger & 0 \end{pmatrix} + \delta_{l0} D_{\mathrm{diag}}, \tag{25}$$

$$(D_{\mathrm{diag}})_{s,\mathbf{n}} = \Delta E_{\mathbf{n}}/\hbar - s\tilde{\delta}/2, \qquad (B_l)_{\mathbf{nm}} = \frac{\Omega_{\mathbf{nm}}}{2} J_{l-q_{\mathbf{nm}}}(A) e^{i(l-q_{\mathbf{nm}})\phi}, \tag{26}$$

where δ_{l0} is the Kronecker delta. These components satisfy $K_{-l} = K_l^\dagger$ and $K_0 = H_F^{(0)}/\hbar$, with $H_F^{(0)}$ given by Eq. (7).

With the time origin fixed at zero, the first correction in the Floquet–Magnus expansion [24,25], $K_F^{(1)} = \hat{H}_F^{(1)}/\hbar$, is

$$\begin{aligned} K_F^{(1)} &= -\frac{i}{2T_s}\int_0^{T_s} dt_1 \int_0^{t_1} dt_2 [\widetilde{K}(t_1), \widetilde{K}(t_2)] \\ &= \sum_{l=1}^{\infty} \frac{[K_l, K_{-l}] + [K_0, K_l - K_{-l}]}{l\omega_s}, \qquad T_s = 2\pi/\omega_s. \end{aligned} \tag{27}$$

Evaluating the commutators gives the coefficients in Eq. (8):

$$\begin{aligned}\alpha^{(e)}_{\mathbf{nm}} =& \sum_{\mathbf{p}}\sum_{l=1}^{\infty}\frac{\Omega_{\mathbf{np}}\Omega^{*}_{\mathbf{pm}}}{4\omega_s l}e^{-iq_{\mathbf{nm}}\phi}\Big[\left(-J_{-q_{\mathbf{np}}+l}J_{q_{\mathbf{pm}}}+J_{-q_{\mathbf{np}}}J_{q_{\mathbf{pm}}-l}\right)e^{il\phi}\\ &+\left(J_{-q_{\mathbf{np}}-l}J_{q_{\mathbf{pm}}}-J_{-q_{\mathbf{np}}}J_{q_{\mathbf{pm}}+l}\right)e^{-il\phi}\\ &+\left(J_{-q_{\mathbf{np}}+l}J_{q_{\mathbf{pm}}+l}-J_{-q_{\mathbf{np}}-l}J_{q_{\mathbf{pm}}-l}\right)\Big], \end{aligned} \tag{28}$$

$$\begin{aligned}\alpha^{(g)}_{\mathbf{nm}} =& \sum_{\mathbf{p}}\sum_{l=1}^{\infty}\frac{\Omega^{*}_{\mathbf{np}}\Omega_{\mathbf{pm}}}{4\omega_s l}e^{-iq_{\mathbf{nm}}\phi}\Big[\left(-J_{q_{\mathbf{np}}-l}J_{-q_{\mathbf{pm}}}+J_{q_{\mathbf{np}}}J_{-q_{\mathbf{pm}}+l}\right)e^{il\phi}\\ &+\left(J_{q_{\mathbf{np}}+l}J_{-q_{\mathbf{pm}}}-J_{q_{\mathbf{np}}}J_{-q_{\mathbf{pm}}-l}\right)e^{-il\phi}\\ &+\left(J_{q_{\mathbf{np}}-l}J_{-q_{\mathbf{pm}}-l}-J_{q_{\mathbf{np}}+l}J_{-q_{\mathbf{pm}}+l}\right)\Big], \end{aligned} \tag{29}$$

$$\beta_{\mathbf{nm}} = \sum_{l=1}^{\infty}\frac{\Omega_{\mathbf{nm}}}{2\omega_s l}\left[J_{-q_{\mathbf{nm}}-l}e^{-i(q_{\mathbf{nm}}+l)\phi}-J_{-q_{\mathbf{nm}}+l}e^{-i(q_{\mathbf{nm}}-l)\phi}\right]. \tag{30}$$

At integer multiples of T_s, $R(t) = R(0)$. The propagator through first order in the frame of Eq. (5) is therefore $R(0)\exp[-i(K_0 + K_F^{(1)})t]R^{\dagger}(0)$.

B Effect of frequency modulation on the probe shift coefficient

For fixed polarization, the period-averaged differential polarizability under frequency modulation is

$$\Delta\alpha_{\text{eff}} = \sum_l J_l^2(A)\Delta\alpha(\nu_c + l\nu_s), \qquad \nu_c = \frac{\omega_c}{2\pi}, \tag{31}$$

where $\Delta\alpha(\nu_{\text{opt}})$ is the differential polarizability between the two clock states at optical frequency ν_{opt}, and ν_c is the carrier frequency in hertz. The sideband power weights satisfy $\sum_l J_l^2(A) = 1$, so the total intensity is unchanged. The probe shift coefficient under modulation, denoted by C_{eff}, is proportional to $\Delta\alpha_{\text{eff}}$. Symmetric sidebands cancel the first-order dispersion term, since $\sum_l l J_l^2(A) = 0$. Expanding the sideband polarizabilities about the carrier frequency to second order and using $\sum_l l^2 J_l^2(A) = A^2/2$, we obtain the leading relative correction:

$$\epsilon_C \equiv \frac{C_{\text{eff}} - C_{\text{probe}}}{C_{\text{probe}}} \simeq \frac{A^2\nu_s^2}{4}\frac{\Delta\alpha''(\nu_c)}{\Delta\alpha(\nu_c)}. \tag{32}$$

The double prime denotes the second derivative with respect to frequency in hertz.

The sideband sum is evaluated with a scalar background polarizability model using the parameter values reported for all 29 transitions in the PTB dataset associated with Lisdat *et al.* [37]. The model includes constant core and core–valence corrections [38]. Within this model, the magnitude of the relative correction, $|\epsilon_C|$, remains below 3×10^{-17} over $0 \le A \le 2.5$ and $0 \le \nu_s \le 30$ kHz.

C Parameters and numerical verification

Table 2 lists the physical parameters and the principal numerical settings for the spectra and the thermal operating map.

The Gaussian standing-wave potential is $V_{\text{lat}}(x, y, z) = -V_0 \exp[-2(x^2 + y^2)/w_0^2]\cos^2(k_l z)$, where $k_l = 2\pi/\lambda_l$. Its harmonic trap frequencies are $\omega_z = k_l\sqrt{2V_0/m}$ and $\omega_r = 2\sqrt{V_0/m}/w_0$. We approximate the

Table 2: Physical and numerical parameters for the motional calculations; the two clock states are retained for every axial basis state.

Parameter	Value or definition
^{87}Sr atomic mass	$m = 1.44315586525 \times 10^{-25}$ kg
Lattice/probe wavelengths	$\lambda_l = 813.43$ nm; $\lambda_p = 698$ nm
Recoil energy	$E_r = \hbar^2(2\pi/\lambda_l)^2/(2m)$; $E_r/h \simeq 3469.54$ Hz
Depth and beam waist	$V_0 = 70E_r$; $w_0 = 30$ μm ($1/e^2$ intensity radius)
Trap frequencies	$\omega_z/(2\pi) \simeq 58.0566$ kHz; $\omega_x/(2\pi) = \omega_y/(2\pi) = \omega_r/(2\pi) \simeq 354.31$ Hz
Lamb–Dicke parameters	$\eta_j = (2\pi/\lambda_p)\sqrt{\hbar/(2m\omega_j)}$ ($j = x, y, z$); $\eta_z = 0.28489$; $\eta_x = 3.64677$
Probe–lattice angular mismatch	$\Delta\theta = 0$, hence $\eta_x\Delta\theta = 0$
Thermal initial state	$\lvert g, n_z = 0\rangle$ at each radial shell n_r, with degeneracy $n_r + 1$ and $T_r = 0.5$ μK
Single-state spectra	$\lvert g, n_z = 0, n_r = 0\rangle$ for Figs. 2 and 3a
Thermal phase and pulse time	$\phi = \pi/2$; $t = 1$ s
Thermal map basis and time step	$n_z = 0, \ldots, 3$; $n_r = 0, \ldots, 400$; $N_t = 4000$ midpoint steps per period, $\Delta t = 1/(N_t\nu_s)$

motional energies by

$$E_{\mathbf{n}} = E_{n_z,n_r} = \hbar\omega_z(n_z + \tfrac{1}{2}) + \hbar\omega_r(n_r + 1) - \frac{E_r}{2}(n_z^2 + n_z + \tfrac{1}{2}) - E_r\frac{\omega_r}{\omega_z}(n_z + \tfrac{1}{2})(n_r + 1), \tag{33}$$

with a common constant omitted. The calculation uses harmonic oscillator probe matrix elements, and numerical convergence is assessed within this approximate energy model.

Perfect alignment conserves the radial quantum numbers during interrogation, but both radial dimensions contribute to the energy and thermal degeneracy. The normalized radial weights at upper shell cutoff M and the thermally averaged spectrum are

$$p_{n_r} = \frac{(n_r + 1)e^{-(E_{0,n_r} - E_{0,0})/(k_B T_r)}}{\sum_{j=0}^{M}(j + 1)e^{-(E_{0,j} - E_{0,0})/(k_B T_r)}}, \qquad P(\nu) = \sum_{n_r=0}^{M} p_{n_r} P_{n_r}(\nu). \tag{34}$$

Here, k_B is the Boltzmann constant and $P_{n_r}(\nu)$ is the excitation spectrum for an individual radial shell with initial state $\lvert g, n_z = 0, n_r\rangle$. All shells share the same modulation depth A. We determine the peak height and the central zero of the error signal from the thermally averaged spectrum $P(\nu)$, keeping the sampling offset fixed.

For the thermal map in Fig. 3c, we sample $\Omega_0/(2\pi) = 100$–1000 Hz in steps of 100 Hz and $\nu_s = 1$–30 kHz in steps of 200 Hz, retaining 1445 points with $\Omega_0/\omega_s \leq 1/2$. The propagator over one modulation period is constructed with the exponential midpoint rule and raised to the integer power $t\nu_s$, the number of modulation periods in the pulse. Local Chebyshev interpolation of the propagator over one modulation period accelerates searches over modulation depth and detuning.

We locally optimize the common modulation depth A to maximize the selected central peak at fixed $t = 1$ s. The peak optimization uses local interpolation checked against direct propagation, with a stopping tolerance of 10^{-9} in A. We solve Eq. (10) on the selected central branch and check the spectral slopes at the two sampling

frequencies using centered finite differences with steps of 0.0005 and 0.00025 Hz. At representative operating and motional resonance points, we compare interpolated and directly propagated excitation probabilities using a tolerance of 10^{-8}. Each directly checked root is enclosed in a frequency interval with a half-width of 0.1 μHz.

To check convergence, we refine the basis and time step while holding fixed the modulation depth calibrated for the map. With the sampling offset held fixed, each calculation determines the central zero of the error signal and the slopes at its two sampling frequencies. We require

$$|\delta\nu_{\mathrm{FE}}^{(1)} - \delta\nu_{\mathrm{FE}}^{(2)}| + h_c^{(1)} + h_c^{(2)} \leq 10\ \mu\mathrm{Hz}, \qquad \max_{j=L,R} \frac{|s_j^{(1)} - s_j^{(2)}|}{|s_j^{(2)}|} \leq 10^{-4}, \tag{35}$$

where s_L and s_R denote the spectral slopes at the left and right sampling frequencies, setting 2 is the finer calculation, and h_c is the half-width of the interval used to localize the center. Table 3 reports these comparisons at fixed A for five representative operating points.

Table 3: Convergence checks at fixed A; $(n_{z,\max}, M, N_t)$ specifies the inclusive axial and radial cutoffs and steps per period, and the center bound includes both localization half-widths.

$(\Omega_0/(2\pi), \nu_s)$	Baseline	Refined	Center bound	Slope change
(Hz, kHz)	$(n_{z,\max}, M, N_t)$	$(n_{z,\max}, M, N_t)$	(μHz)	(%)
$(500, 1)$	$(3, 400, 4000)$	$(4, 600, 8000)$	0.20000	0.00246
$(500, 16.8)$	$(3, 400, 4000)$	$(4, 600, 8000)$	0.23550	0.00232
$(1000, 27.2)$	$(3, 400, 4000)$	$(4, 600, 8000)$	0.45874	0.00497
$(500, 30)$	$(3, 400, 4000)$	$(4, 600, 8000)$	0.22066	0.00233
$(1000, 11.4)$	$(3, 400, 4000)$	$(4, 600, 8000)$	0.21937	0.00500

In table order, the modulation depths are approximately 2.33462, 2.40260, 2.40285, 2.40272, and 2.40180, and all five comparisons satisfy the adopted criteria.

For the spectra and phase scan from a single initial state in Fig. 2, we use the axial basis $n_z = 0, \ldots, 3$. We integrate the propagator over one modulation period using an adaptive eighth-order Runge–Kutta method (DOP853), with relative tolerance 2×10^{-12} and absolute tolerance 2×10^{-14}. For the spectra near motional resonances in Fig. 3a, we retain $n_z = 0, \ldots, 4$ and use tolerances 2×10^{-13} and 2×10^{-15}. An integer matrix power propagates the complete modulation periods; any remaining fraction of a period is propagated separately.

For the phase scan in Fig. 2b, we fix $A = 2.2$ and locally maximize the excitation probability at zero detuning and $\phi = \pi/2$ over pulse durations containing an integer number of modulation periods. We follow the same local maximum as the probe power increases. The selected duration and the corresponding sampling offset for an ideal Rabi pulse are used for every phase at that power. The scan covers $\Omega_0/(2\pi) = 100$–1500 Hz in steps of 10 Hz. Retaining the first power setting for each distinct duration gives 96 settings spanning $\Omega_0/(2\pi) = 100$–1460 Hz, with 33–472 periods (3.3–47.2 ms). The seven phases give 672 phase/power combinations.

For each phase, we fit

$$\delta\nu_{\mathrm{FE}} = b_\phi + k_\phi u, \qquad u = \frac{\Omega_0^2/\omega_s}{2\pi}, \tag{36}$$

with a free intercept using 96 data points per phase. Table 4 lists the fitted slopes and their standard errors, which are derived from the fit residuals and quantify deterministic deviations from the linear fit.

Table 4: Dimensionless fitted slopes of Fig. 2b and their standard errors derived from the fit residuals.

ϕ	k_ϕ	Standard error
0	-0.10402	1.0971×10^{-4}
$\pi/4$	-0.06034	6.1978×10^{-5}
$3\pi/8$	-0.02820	2.8813×10^{-5}
$\pi/2$	2.1927×10^{-7}	6.3262×10^{-7}
$5\pi/8$	0.02820	2.9102×10^{-5}
$3\pi/4$	0.06034	6.2314×10^{-5}
π	0.10402	1.1012×10^{-4}

Repeating all 672 combinations with $n_z = 0, \ldots, 4$ and tolerances 5×10^{-14} and 5×10^{-16} changes centers by at most 0.12831 μHz and fitted slopes by at most 9.17×10^{-11}.

The bound $|k_{\pi/2}| < 10^{-6}$ quantifies suppression of the power-dependent shift in this scan. To obtain this bound, we use the checked numerical configurations and propagate the intervals enclosing the roots of the error signal to the fitted slope.

D Coupling matrix element between motional states

For small $\Delta\theta$, the coupling matrix element is

$$\Omega_{\mathbf{nm}} = \Omega_0 \langle n_x | D_x(i\eta_x \Delta\theta) | m_x \rangle \delta_{n_y, m_y} \langle n_z | D_z(i\eta_z) | m_z \rangle. \tag{37}$$

The operators D_x and D_z are displacement operators along the x and z directions, respectively.

For the imaginary displacement arguments used here, the harmonic oscillator coupling matrix is complex symmetric, $\Omega_{\mathbf{nm}} = \Omega_{\mathbf{mn}}$. The two off-diagonal blocks that couple the clock states in Eq. (5) are Hermitian conjugates, ensuring that the full Hamiltonian is Hermitian.

E Two-point uncertainty model and numerical validation

At power j, let $P_j(\nu; \boldsymbol{z}_a)$ denote the thermally averaged excitation spectrum for the left ($a = L$) or right ($a = R$) sampling pulse, before its fluctuating Stark shift is applied. The detuning ν is measured from the probe-shifted transition at the set power. The vector $\boldsymbol{z}_a$ contains the parameter noise variables for pulse a, and $\boldsymbol{z}_a = \mathbf{0}$ corresponds to the set parameter values. Shell probabilities are averaged before determining the two-point root and its noise derivatives.

We write the offset as $\xi_j(C, \boldsymbol{z}_j)$, where $\boldsymbol{z}_j$ contains the independent standard normal noise variables of both pulses. The value $\xi_{j,0} = \xi_j(C, \mathbf{0})$ is the frequency offset when all pulse parameters take their set values.

For pulse parameter noise, we write $\boldsymbol{z}_j = (\boldsymbol{z}_R^\mathsf{T}, \boldsymbol{z}_L^\mathsf{T})^\mathsf{T}$, suppressing the power index on the pulse subvectors. The bare Rabi frequency is $\Omega_{j,a} = \Omega_j(1 + r_\Omega z_{\Omega,j,a})$, where $z_{\Omega,j,a}$ is the standard normal variable for its fluctuation. The phase and modulation depth deviations are obtained by multiplying the corresponding standard normal variables by σ_ϕ and σ_A, respectively. The additional Stark shift caused by the power fluctuation is

$$S_{j,a}(C) = C\Omega_j^2 \big(2 r_\Omega z_{\Omega,j,a} + r_\Omega^2 z_{\Omega,j,a}^2\big). \tag{38}$$

We determine ξ_j from the zero of the two-point error signal near the central resonance:

$$F_j(\xi_j; C, \boldsymbol{z}_R, \boldsymbol{z}_L) = P_j(\xi_j + \nu_{\mathrm{off},j} - S_{j,R}; \boldsymbol{z}_R) - P_j(\xi_j - \nu_{\mathrm{off},j} - S_{j,L}; \boldsymbol{z}_L) = 0. \tag{39}$$

The thermal weights, pulse duration, sampling offset and nominal pulse parameters are held fixed across noise realizations. During a pulse, each parameter deviation stays constant and has the same value for all radial motional states. The independent Gaussian variables describe the two pulses; within each pulse, the same power fluctuation affects both the spectrum $P_j(\nu; \boldsymbol{z}_a)$ and the Stark shift $S_{j,a}$.

For the detection noise term in Eq. (14), we use the spectrum $P_j(\nu; \mathbf{0})$. At the two sampling frequencies $\xi_{j,0} \mp \nu_{\mathrm{off},j}$, the common excitation probability is P_j^*, and the spectral slopes are $s_{L,j}$ and $s_{R,j}$, respectively. After averaging, the detection fluctuations in the two samples are independent and have the same standard deviation $\sigma_{P,j}$, so $\mathrm{SNR}_j = P_j^*/\sigma_{P,j}$. The two-point frequency conversion factor is

$$\gamma_{\mathrm{eff},j} = \frac{\sqrt{2}\, P_j^*}{|s_{R,j} - s_{L,j}|}. \tag{40}$$

The resulting frequency uncertainty due to detection noise is $\gamma_{\mathrm{eff},j}/\mathrm{SNR}_j = \sqrt{2}\,\sigma_{P,j}/|s_{R,j} - s_{L,j}|$.

We define $\boldsymbol{b}_j$ and Q_j as the gradient and Hessian of ξ_j with respect to $\boldsymbol{z}_j$, evaluated at zero noise. The mean and variance are

$$\langle \xi_j \rangle \simeq \xi_{j,0} + \tfrac{1}{2}\,\mathrm{tr}\,\mathsf{Q}_j, \qquad V_j \simeq \boldsymbol{b}_j^{\mathsf{T}} \boldsymbol{b}_j + \tfrac{1}{2}\,\mathrm{tr}(\mathsf{Q}_j^2). \tag{41}$$

A pulse pair with Floquet modulation has six noise variables, comprising fluctuations in power, phase and modulation depth in each pulse. An unmodulated pulse pair, including the common reference at low probe power, has the two independent power fluctuations.

At zero noise, implicit differentiation gives

$$b_i = -\frac{F_i}{F_\xi}, \qquad \mathsf{Q}_{ik} = -\frac{F_{ik} + F_{\xi i} b_k + F_{\xi k} b_i + F_{\xi\xi} b_i b_k}{F_\xi}, \tag{42}$$

where all derivatives are evaluated at the central root at zero noise and the stage index is omitted. Subscripts ξ and i, k denote partial derivatives with respect to the frequency variable ξ and the components of $\boldsymbol{z}_j$, respectively. The estimated frequency depends nonlinearly on the fluctuations in both pulses, so mixed derivatives are retained even though the noise variables are independent.

The additional Stark shift is proportional to C, so the second-order expansion gives terms up to C^2 in the mean offset difference $\langle \xi_{\mathrm{high}} \rangle - \langle \xi_{\mathrm{low}} \rangle$. When solving Eq. (13), we select the root close to a preliminary estimate of C_{probe}.

For the calibration contribution, we use the first-order response to a fractional Rabi frequency error shared by the two sampling pulses. The resulting contribution to the variance of the frequency difference is

$$V_{\mathrm{cal}} = r_{\mathrm{cal}}^2 (g_{\mathrm{high}}^2 + g_{\mathrm{low}}^2), \qquad g_j = (b_{\Omega,j,R} + b_{\Omega,j,L})/r_\Omega. \tag{43}$$

Here, $b_{\Omega,j,R}$ and $b_{\Omega,j,L}$ are the components of $\boldsymbol{b}_j$ associated with Rabi frequency fluctuations in the right and left sampling pulses, respectively. Because $\boldsymbol{b}_j$ is defined with respect to standard normal noise variables, dividing the summed pulse responses by r_Ω gives the response g_j to a shared fractional Rabi frequency error, including its Stark and spectral effects.

For Fig. 4, we sample $\Omega_{\mathrm{high}}/(2\pi) = 20$–$1000$ Hz in steps of 10 Hz, giving 99 settings for the high probe power. At each setting, we select the common modulation depth A at a local maximum of the thermally averaged central peak for fixed $t = 1$ s. The modulation frequency is $\nu_s = 11.4$ kHz, with the mass and noise parameters given in Table 1.

We retain the axial basis $n_z = 0, \ldots, 3$ separately for each radial shell $n_r = 0, \ldots, 400$. Each shell starts in $n_z = 0$, with radial weights given by Eq. (34) at $T_r = 0.5$ μK. The Floquet propagator over one modulation period is integrated with DOP853, using relative and absolute tolerances of 2×10^{-13} and 2×10^{-15}, respectively. Its 11400th matrix power gives the propagator for the pulse lasting 1 s. For the conventional Rabi reference, the static Hamiltonian is diagonalized in the same basis, and the state is propagated for $t_j = \pi/\Omega_j$.

We check how the standard deviation of the frequency estimate due to noise in the pulse parameters depends on the differentiation step. The base step in detuning is $0.005/t_j$. The steps in the standard normal variables for Rabi frequency, phase and modulation depth are 1, 4 and 8, respectively. This check covers all 99 settings for the high probe power and the common reference at low probe power. The two estimates obtained by Richardson extrapolation from steps scaled by 1/2, 1 and 2 differ by at most $5.4 \times 10^{-6}\%$.

We check the basis and integration accuracy at $\Omega_{\mathrm{high}}/(2\pi) = 1000$ Hz and for the common reference at low probe power. With nominal controls fixed, we increase the axial and radial cutoffs to $n_z = 4$ and $n_r = 600$ for both schemes. For Floquet propagation, we also tighten the relative and absolute integration tolerances to 5×10^{-14} and 5×10^{-16}. At this setting of the high probe power, the total coefficient uncertainty changes by at most $3.2 \times 10^{-7}\%$ for either scheme at any of the four calibration levels.

The Monte Carlo comparison below tests the second-order prediction for the standard deviation of the frequency estimate due to noise in the pulse parameters. We use the single initial state $|g, n_z = 0, n_r = 1\rangle$ without thermal averaging. The same two-point estimator is used, with modulation depths calibrated for the response of this radial shell. This separate benchmark uses the numerical parameters of Table 2, with $\nu_s = 11.4$ kHz, $t = 1$ s, $r_\Omega = 10^{-3}$, $\sigma_t = 1$ ns and $\sigma_A = 10^{-6}$.

An independent Monte Carlo calculation uses local interpolation of the propagator over one modulation period, followed by propagation over the full pulse and nonlinear root finding for the two-point error signal. Its interpolation accuracy is checked with separately propagated noise realizations. For each realization, we draw independent fluctuations in power, phase and modulation depth for the two pulses and keep the sampling offset fixed. Table 5 compares the resulting standard deviations with the second-order prediction. All five predictions lie within the 95% bootstrap intervals from 10000 samples.

The reported standard deviation describes the spread of frequency estimates from individual pulse pairs. Larger sample sizes provide a more precise estimate of this standard deviation.

Table 5: Independent sampling check of the frequency standard deviation $\sigma_{\mathrm{par}} = \sqrt{V_{\mathrm{high}}}$ due to noise in the pulse parameters. The Floquet benchmark uses one radial shell and includes direct Stark shift fluctuations. The intervals are 95% percentile bootstrap intervals obtained from 2000 resamples of the $N = 10000$ estimates from pulse pairs.

$\Omega_{\mathrm{high}}/(2\pi)$ (Hz)	Second order (mHz)	$N = 100$ (mHz)	$N = 1000$ (mHz)	$N = 10000$ (mHz)	95% interval (mHz)
20	0.07122	0.06942	0.07245	0.07088	[0.06992, 0.07191]
100	0.34222	0.34173	0.34772	0.34333	[0.33866, 0.34806]
300	3.01558	3.56981	3.07311	3.02041	[2.97644, 3.06157]
500	8.37478	7.52262	8.17012	8.33832	[8.22135, 8.45157]
1000	33.49931	32.50911	33.65916	33.43552	[32.99441, 33.90304]

References

[1] Ludlow A D, Boyd M M, Ye J, Peik E and Schmidt P O 2015 *Reviews of Modern Physics* **87** 637–701 URL `https://doi.org/10.1103/RevModPhys.87.637`

[2] Bloom B J, Nicholson T L, Williams J R, Campbell S L, Bishof M, Zhang X, Zhang W, Bromley S L and Ye J 2014 *Nature* **506** 71–75

[3] Nicholson T L, Campbell S L, Hutson R B, Marti G E, Bloom B J, McNally R L, Zhang W, Barrett M D, Safronova M S, Strouse G F, Tew W L and Ye J 2015 *Nature Communications* **6** 6896

[4] McGrew W F, Zhang X, Fasano R J, Schäffer S A, Beloy K, Nicolodi D, Brown R C, Hinkley N, Milani G, Schioppo M, Yoon T H and Ludlow A D 2018 *Nature* **564** 87–90 URL `https://doi.org/10.1038/s41586-018-0738-2`

[5] Ushijima I, Takamoto M, Das M, Ohkubo T and Katori H 2015 *Nature Photonics* **9** 185–189

[6] Campbell S L, Hutson R B, Marti G E, Goban A, Darkwah Oppong N, McNally R L, Sonderhouse L, Robinson J M, Zhang W, Bloom B J and Ye J 2017 *Science* **358** 90–94

[7] Bothwell T, Kedar D, Oelker E, Robinson J M, Bromley S L, Tew W L, Ye J and Kennedy C J 2019 *Metrologia* **56** 065004

[8] Oelker E, Hutson R B, Kennedy C J, Sonderhouse L, Bothwell T, Goban A, Kedar D, Sanner C, Robinson J M, Marti G E, Matei D G, Legero T, Giunta M, Holzwarth R, Riehle F, Sterr U and Ye J 2019 *Nature Photonics* **13** 714–719

[9] Takamoto M, Ushijima I, Ohmae N, Yahagi T, Kokado K, Shinkai H and Katori H 2020 *Nature Photonics* **14** 411–415

[10] Aeppli A, Kim K, Warfield W, Safronova M S and Ye J 2024 *Physical Review Letters* **133** 023401

[11] Huntemann N, Lipphardt B, Tamm C, Gerginov V, Weyers S and Peik E 2014 *Physical Review Letters* **113** 210802 URL `https://doi.org/10.1103/PhysRevLett.113.210802`

[12] Safronova M S, Budker D, DeMille D, Kimball D F J, Derevianko A and Clark C W 2018 *Reviews of Modern Physics* **90** 025008

[13] Chou C W, Hume D B, Rosenband T and Wineland D J 2010 *Science* **329** 1630–1633 URL https://doi.org/10.1126/science.1192720

[14] Delva P *et al.* 2017 *Physical Review Letters* **118** 221102

[15] Yudin V I, Taichenachev A V, Oates C W, Barber Z W, Lemke N D, Ludlow A D, Sterr U, Lisdat C and Riehle F 2010 *Physical Review A* **82** 011804 URL https://link.aps.org/doi/10.1103/PhysRevA.82.011804

[16] Huntemann N, Lipphardt B, Okhapkin M, Tamm C, Peik E, Taichenachev A V and Yudin V I 2012 *Physical Review Letters* **109** 213002 URL https://link.aps.org/doi/10.1103/PhysRevLett.109.213002

[17] Hobson R, Bowden W, King S A, Baird P E G, Hill I R and Gill P 2016 *Physical Review A* **93** 010501

[18] Sanner C, Huntemann N, Lange R, Tamm C and Peik E 2018 *Physical Review Letters* **120** 053602

[19] Zanon-Willette T, Lefevre R, Metzdorff R, Sillitoe N, Almonacil S, Minissale M, de Clercq E, Taichenachev A V, Yudin V I and Arimondo E 2018 *Reports on Progress in Physics* **81** 094401

[20] Leibrandt D R, Porsev S G, Cheung C and Safronova M S 2024 *Nature Communications* **15** 5663

[21] Huang Y, Guan H, Liu P, Bian W, Ma L, Liang K, Li T and Gao K 2016 *Physical Review Letters* **116** 013001

[22] Goldman N and Dalibard J 2014 *Physical Review X* **4** 031027 URL https://doi.org/10.1103/PhysRevX.4.031027

[23] Eckardt A and Anisimovas E 2015 *New Journal of Physics* **17** 093039 URL https://iopscience.iop.org/article/10.1088/1367-2630/17/9/093039

[24] Bukov M, D'Alessio L and Polkovnikov A 2015 *Advances in Physics* **64** 139–226

[25] Eckardt A 2017 *Reviews of Modern Physics* **89** 011004

[26] Mikami T, Kitamura S, Yasuda K, Tsuji N, Oka T and Aoki H 2016 *Physical Review B* **93** 144307

[27] Rahav S, Gilary I and Fishman S 2003 *Physical Review A* **68** 013820

[28] Xu Q F, Lu X T, Xia J J, Wang Y B and Chang H 2021 *Applied Physics Letters* **119** 101105

[29] Yin M J, Wang T, Lu X T, Li T, Wang Y B, Zhang X F, Li W D, Smerzi A and Chang H 2021 *Chinese Physics Letters* **38** 073201

[30] Lu X T, Wang T, Li T, Zhou C H, Yin M J, Wang Y B, Zhang X F and Chang H 2021 *Physical Review Letters* **127** 033601

[31] Yin M J, Lu X T, Li T, Xia J J, Wang T, Zhang X F and Chang H 2022 *Physical Review Letters* **128** 073603

[32] Liu W X, Lu X T, Li T, Zhang X F, Chang H, Wang T and Li W D 2023 *Physical Review A* **107** 013315

[33] Lu X T, Guo F, Wang Y B, Xu Q F, Zhou C H, Xia J J, Wu W J and Chang H 2023 *Metrologia* **60** 015008

[34] Guo F, Zhou Y H, Liu Y Y, Li J A, Lu X T, Zhao Y T and Chang H 2025 *Communications Physics* **8** 442 URL https://doi.org/10.1038/s42005-025-02341-5

[35] Ye J, Kimble H J and Katori H 2008 *Science* **320** 1734–1738 URL https://www.science.org/doi/abs/10.1126/science.1148259

[36] Al-Masoudi A, Dörscher S, Häfner S, Sterr U and Lisdat C 2015 *Physical Review A* **92** 063814

[37] Lisdat C, Dörscher S, Nosske I and Sterr U 2021 *Physical Review Research* **3** L042036 accompanying data: doi:10.7795/720.20210928 URL https://journals.aps.org/prresearch/abstract/10.1103/PhysRevResearch.3.L042036

[38] Safronova M S, Porsev S G, Safronova U I, Kozlov M G and Clark C W 2013 *Physical Review A* **87** 012509 URL https://journals.aps.org/pra/abstract/10.1103/PhysRevA.87.012509